Chapter 17
Imaging the Interaction of Electrical Currents with Magnetization Distributions

Robert Frömter, Edna C. Corredor, Sebastian Hankemeier, Fabian Kloodt-Twesten, Susanne Kuhrau, Fabian Lofink, Stefan Rößler and Hans Peter Oepen

17.1 Introduction

About a decade ago, the understanding of the interaction mechanisms between electrical currents and magnetic objects like domain walls or vortices was still in its infancy. Both, theory and experiments were moving on uncharted grounds, with new and many times contradicting results being published from different groups at increasing pace. Previously, only the Oersted field from a current was available to manipulate the magnetic state of a system. The latter was extensively used in magnetic storage devices, starting from the early core memory up to the write heads of the latest hard drive technologies based on perpendicular recording and tunnel-magnetoresistive (TMR) readout sensors, to alter the state of the magnetic bits. Even early prototypes of magnetic random-access memory (MRAM) used the Oersted field for writing.

17.1.1 Spin-Transfer Torque

With the experimental confirmation of the spin-transfer-torque (STT) effect in magnetic wires [1–4] a new method for manipulating magnetic bits became available. The STT arises, when an electrical current passes a boundary between regions (domains) of different magnetization orientation like, e.g. a domain wall in a magnetic wire with in-plane magnetization. In a simple picture for a 3d ferromagnet like Co

R. Frömter (✉) · E. C. Corredor · S. Hankemeier · F. Kloodt-Twesten ·
S. Kuhrau · F. Lofink · S. Rößler · H. P. Oepen
Institut für Nanostruktur- und Festkörperphysik,Universität Hamburg, Hamburg, Germany
e-mail: rfroemte@physik.uni-hamburg.de

H. P. Oepen
e-mail: oepen@physik.uni-hamburg.de

or Fe, the s-like conduction electrons are spin polarized by the itinerant 3d electrons that carry the magnetization via s-d scattering processes. While crossing the domain wall the conduction electrons constantly adjust their polarization to the locally altered magnetization direction. The conservation of spin angular momentum in turn rotates the localized moments by a certain degree into the opposite direction, thus gradually moving the wall along the electron current direction. The efficiency of this process is characterized by the so-called spin-drift velocity. To manipulate a magnetization distribution in this way has two consequences that stirred the excitement in the magnetism community: First, the local action of a current in a magnetic wire or multilayer stack promised potential for miniaturization of devices like STT-MRAM, in contrast to the far-reaching Oersted field from separate current carrying wires, where cross-talk had to be circumvented by size. Also, the energy required for switching could be strongly reduced for an efficient material, making it interesting for mobile devices. Second, if a wire with alternating up-down or left-right domains is exposed to STT all domain walls are pushed into the same direction, whereas when applying an Oersted field the domains alternatingly shrink or grow. This led to the proposal of the so-called racetrack memory [5], a domain-wall shift register that, if successfully extended into the third dimension, could satisfy future storage-density needs.

Following early theoretical predictions by Berger [6] and Slonczewski [7], a micromagnetic model for describing the effect of the local current density on the local magnetization was developed in 2004 [8–10]. It consists of two additional current-dependent terms in the Landau-Lifshitz-Gilbert (LLG) equation, describing both, an adiabatic and a non-adiabatic contribution. The degree of nonadiabaticity is denoted by the parameter β. It was thought to originate mainly from spin relaxation, namely a miss-tracking of itinerant electrons with respect to the domain wall profile, leading to transverse spin accumulation. The importance of β is that the non-adiabatic torque acts like a negative damping term to the adiabatic torque, thus a large value will increase the domain wall velocity under current. Simulations predict that the initial domain wall velocity is strongly increased for $\beta > \alpha$, the latter being the Gilbert damping constant in LLG. Thus, a high-β material would have significant technological advantage. Unfortunately, it turned out to be experimentally very difficult to measure β and the reported values, even for the best-studied material at that time, permalloy, varied by orders of magnitude. In Sect. 17.2 an experiment is explained in more detail, where we measured the β parameter of permalloy with unprecedented accuracy, following a proposal from theory [11]. It is based on measuring the equilibrium displacement of a vortex in a permalloy square under direct current flow. The result of the analysis led to the unexpected conclusion, that the micromagnetic model used to describe the current-vortex interaction was not yet complete [12]. An additional, nonlocal contribution to the non-adiabatic STT has to be included to correctly describe the strong magnetization gradients occurring in tiny objects like magnetic vortices.

17.1.2   *SEMPA as a Unique Tool for Magnetic Imaging*

To carry out magnetization imaging we use the Scanning Electron Microscope with Polarization Analysis (SEMPA), which we have developed in our group and keep adding features, like recently the time resolution, which is discussed in more detail in Sect. 17.4. SEMPA is based on the effect that the secondary electrons that are emitted during image formation in a scanning electron microscope (SEM) carry with their spin the information about the magnetization at the surface area they originated from. Thus, by measuring the spin polarization of the secondary electrons a map of the surface magnetization is obtained. To measure the spin-polarization we use spin-polarized low-energy electron diffraction (SPLEED) at a tungsten single crystal, where at 104.5 eV the (2, 0) beams show an intensity asymmetry depending on the spin-polarization of the incoming electrons. A sketch of the setup is shown in Fig. 17.1. As there are four (2, 0) beams in the LEED pattern, two orthogonal components of the spin polarization can be measured simultaneously, which allows for the parallel acquisition of two orthogonal magnetization components in the sample surface. As the information depth for the initial process of spin polarization is very small (only about 0.5 nm in iron) and LEED is also very surface sensitive, SEMPA is necessarily an ultrahigh-vacuum (UHV) experiment. This allows to carry out clean surface-science experiments on uncapped epitaxial magnetic layers to study ideal material properties. But also ex-situ prepared samples can be analyzed following some surface treatment like Co- or Fe-atom decoration or mild Ar-ion sputtering in a Kaufman-type source. We have found that some cappings like graphene are even stable to atmosphere and still magnetically transparent [13].

Key features of our SEMPA setup are: A lateral resolution of down to 10 nm can be obtained using 5 nA primary beam current at 5 keV kinetic energy. Both in-plane components of the surface magnetization are imaged simultaneously. With standard image quality, for each pixel an angular accuracy <4° for determining the magnetization orientation is obtained. A second setup allows for imaging the out-of-plane component together with one in-plane component by using a 90° electrostatic deflector (cylindrical mirror analyzer) in front of the spin detector. The sample temperature can be varied continuously from 40–400 K using a liquid-helium cryostat coupled to the sample holder. An in-situ coil on a ferrite core with gap allows to apply magnetic fields up to 60 mT at the sample. The working pressure of the microscope is below 5×10^{-11} mbar, which allows for several days of analysis by maintaining a sufficiently clean surface. A sample preparation chamber with surface science equipment like LEED and Auger electron spectroscopy is directly attached. In addition, ex-situ prepared samples can be transferred in and out of UHV by means of a fast-entry lock. Several thermal evaporators for in-situ contrast enhancement with clean ferromagnetic layers, as well as sputter sources for Ar-ion cleaning at different energies from 100–2000 eV are installed directly in the microscope chamber. Coaxial electrical wires and matched contacts to the sample allow for high-frequency stimulation up to several GHz or, alternatively, for in-situ four-point-probe measurements of sample resistivity. Acquisition times from 10 min (for regular images) to several hours (for
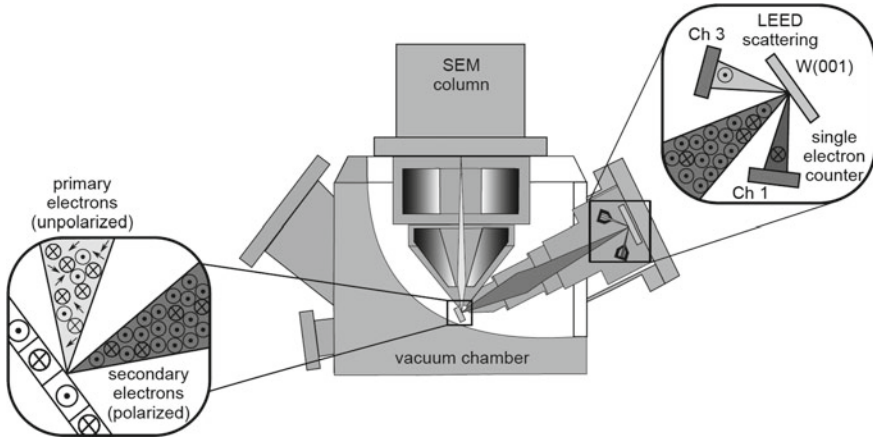
Fig. 17.1 Essentials of SEMPA. In the center a schematic of the setup is shown, consisting primarily of the SEM column and the spin detector in a UHV chamber. The two insets illustrate the main processes involved: To the left, the generation of spin-polarized secondary electrons at the surface of a magnetic sample is shown and to the right the tungsten-based SPLEED detector that yields an intensity asymmetry of opposed (2, 0) beams as function of the spin-polarization of the incoming beam. Of the four channels recorded, only the detector pair in the paper plane is shown. An electron optics between sample and tungsten crystal serves to efficiently pick up the secondary electrons, as well as to collimate and align the beam of secondary electrons with the correct energy onto the crystal (from [14])

time-resolved imaging) are feasible using digital drift correction. A time resolution of 700 ps has been demonstrated.

A more general review of the technique can be found in [15]. Details on our setup including a method to calculate and optimize the detection efficiency are given in [16]. The long-time stability of the SPLEED detector used for spin analysis against residual gas contamination is analyzed in [17]. The latest technical contribution is the introduction of nanosecond time resolution to SEMPA [18], which will be described in more detail in Sect. 17.4.

17.2 Determining the Nonadiabaticity Parameter from the Displacement of Magnetic Vortices

As described in the introduction, the parameter β that quantifies the amount of non-adiabaticity in STT turned out to be hard to measure experimentally. The reason for this was obvious, as most experiments attempted to derive β from the critical current density required to initiate domain wall motion in a magnetic wire. For a non-ideal system with possibly some amount of edge roughness and internal grain structure, however, this critical current density is more related to the local pinning landscape

than to intrinsic material properties. In addition, the type of domain wall was not necessarily well-defined, as transitions under STT were observed. Thus published values varied over orders of magnitude.

17.2.1 Proposal from Theory

After developing a description for confined magnetic vortices under STT and external field using the Thiele model [19], a proposal to use the current-induced displacement of the magnetic vortex in the Landau state of a square magnetic element came up to determine β [11]. It was shown that the four degenerate ground states (polarity $p = \pm 1$ and curl $c = \pm 1$) of the Landau state behave differently under the various torques. While the non-adiabatic contribution and the Oersted field of the current shift the vortex in the axis of the current direction, the adiabatic contribution shifts the vortex orthogonal to the current. The amount of displacement against the parabolic confinement can be used like a balance to measure the strengths of the individual contributions from a comparison of displacements for the different ground states. As the vortex stays close to the center, an influence of edge roughness can be excluded. The extended period of time during which the vortex is exposed to a constant drive current will reduce pinning at grains, as the system can gradually creep into its stationary equilibrium. In this way, frequent problems of other methods can be avoided.

17.2.2 Sample Preparation

In order to realize such an experiment in SEMPA, several challenges had to be faced. To obtain well observable displacements of the order of 100 nm in a $5\,\mu\mathrm{m} \times 5\,\mu\mathrm{m} \times 12\,\mathrm{nm}$ sized permalloy square, a current density of several 10^{11} A/m^2 is required. In contrast to most common experiments that require only current pulses from nanosecond to microsecond duration, this ultrahigh current density needs to be sustained during the whole time of acquiring an image, which can be several 10 min. During this period, no excessive heating of the structure is allowed. Under normal circumstances any metal wire would soon be destroyed by Joule heating or electromigration. To circumvent this problem we have developed a method to prepare metal wires on synthetic single-crystalline diamond substrates, held at cryogenic temperature. A comparison of low-temperature thermal conductances shows that single-crystalline diamond has the highest thermal conductivity (10^4 W/mK) of all materials at liquid-nitrogen temperature [20], about 20 times higher than copper at room temperature. Still, the purely phononic conductivity does not conduct electrical current, so no shunt is created. The available surface roughness can be below 0.3 nm RMS, as checked by AFM. In a test experiment a 22.5 nm high, 650 nm wide and $25\,\mu\mathrm{m}$ long permalloy wire on diamond was placed in vacuum on a cryostat held
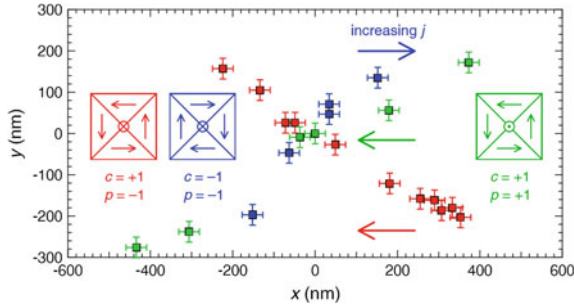
Fig. 17.2 Map of the current-dependent vortex positions in the permalloy square for the three different ground states illustrated. The current density is varied over a range of $\pm 3 \times 10^{11}$ A/m in the direction indicated for each case. All three states show a reasonably linear behavior, which allows to extract three slopes from the data and to calculate the non-adiabaticity. For details, see [12]

at 100 K. It could withstand a current density of 2×10^{12} A/m^2 for at least an hour without damage [21].

Our attempts to perform lithography on the diamond surface were unsuccessful. We therefore used a stencil mask deposition technique with focused-ion-beam (FIB) machined silicon nitride membranes and optical alignment to prepare the permalloy square and the gold contact pads.

17.2.3 Experimental Results

The experiment has been carried out without attaching the cryostat, so the state without current is at room temperature. Careful analysis of the resistance of the sample while applying the current allows to calculate the sample temperature. The maximum temperature recorded at the maximum current of $\pm 3 \times 10^{11}$ A/m applied was 350 K. As we found no temperature dependence of β over this range [22], thermal effects can be neglected. By using field pulses from an in-situ electromagnet we were able to seed three of the four possible ground states of the permalloy square. This turned out to be sufficient to perform the analysis, as only three unknown torque terms had to be separated. Fig. 17.2 shows the obtained positions of the vortex cores for the three states and for the current ramping from negative to positive values as indicated. Three different linear slopes can be extracted from the dataset, which allow for further analysis. As result we find for the parameter of non-abiaticity $\beta = 0.119 \pm 0.022$ for the permalloy vortex. In addition, the spin drift velocity $v_j = (4.79 \pm 0.26)$ m/s can be directly determined form the slopes. As we also performed ferromagnetic resonance measurements on the material to determine the saturation magnetization, we can give as third material parameter the spin polarization, which is $(65 \pm 4)\%$, and the damping constant $\alpha = 0.0085 \pm 0.0006$.

When comparing this data to results from other groups, one observation was stringent: Two other experiments that also used vortices as test objects showed similarly high values for β [23, 24], albeit with less precision. In contrast, another carefully performed study using spin-wave dispersion instead of vortices resulted in a 5 times smaller value of $\beta = 0.022$ [25]. In fact this value is only about twice as large as α - similar values for both constants have indeed been predicted. As all the other material parameters of our system mentioned above were very similar in this study, the huge difference can only be appointed to the different object investigated. The spin waves analyzed in [25] are of the order of 10 µm in period, whereas vortices have a very narrow core of the order of 10 nm, so the spatial variation of the magnetization takes place on a much smaller length scale. Indeed theory predicts a second [26] truly non-adiabatic contribution to β that is due to spin scattering and that is essentially nonlocal [8]. It is oscillatory in space due to the precession of conduction electron spins [27]. Micromagnetic calculations with a more complex code that accounts for these nonlocal effects have already shown a threefold increase of the effective β for a vortex wall compared to a transverse wall [28]. Our experimental results prove that for small magnetic structures like vortices or skyrmions, which are small on the length scale of the Larmor precession, the local description using the LLG equation with two additional spin torque terms is not sufficient.

17.3   Applications of Vectorial Magnetic Imaging

Magnetic imaging can be performed to solve a variety of different tasks. A standard task is the question if and under which conditions a certain magnetic structure exists or ceases to exist. High-resolution vectorial magnetization imaging, which is possible directly by using SEMPA or following phase retrieval in Lorentz transmission electron microscopy (TEM) [29] or TEM holography [30], can supply a lot more information. The whole magnetization map of a structure becomes available and can be compared to micromagnetic simulations or analytical predictions. Micromagnetic simulations have developed over the last years into a very powerful and easy to use toolkit for predicting micromagnetic structures and devices, even including dynamic effects like STT or "defects" like grain boundaries [31, 32]. In reality, however, magnetic structures often look or behave quite differently. This can be most sensitively tested in a vectorial imaging experiment, as already small angular deviations from the predicted pattern become directly evident. Reasons for such discrepancies can be systematic deviations of the real structure from the one modeled, like the often non-ideal, inclined edges of magnetic wires. There can be defects like kinks resulting from problems in the lithography process of a real structure, that will pin domain wall motion. Stochastic variations of magnetic properties like grain boundaries in a polycrystalline material or surface/interface roughness can act as internal pinning sites. Finite temperature can have a strong impact on the depinning mechanism from those sites. However, for more ideal structures it is often possible to extract numbers for unknown magnetic properties by comparison with simulation. In some cases even
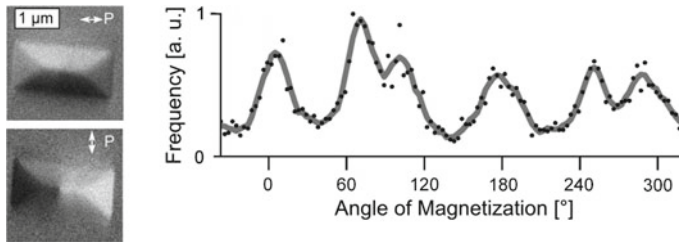
Fig. 17.3 Magnetic fine structure of a permalloy rectangle of size $2\,\mu m \times 1\,\mu m \times 20\,nm$ observed in a vectorial SEMPA polarization map. The angular magnetization histogram to the right reveals that not four but six domains are clearly separated. The splitting of the larger two domains leads to the emergence of stray field and thus enables coupling between such rectangles. For details, see [36]

the magnetic theory behind the simulation may be incomplete and simply predict wrong results.

In several cases we have used the vectorial imaging capability to clarify magnetic ground state properties of various systems. The internal structure of the canted magnetization (also known as cone state) in a continuous Co/Pt multilayer film close to the spin-reorientation transition has been imaged for the first time in [33]. We found a temporally stable isotropic and gradual in-plane modulation, superimposed onto an alternating up/down domain pattern, both modulated on a similar length scale.

A similar study has focussed on the temperature-driven spin-reorientation transition between two different in-plane easy axes in $NdCo_5$, where the temperature-dependent anisotropy could be extracted and the microstructure analyzed [34, 35].

A third study deals with the internal magnetic structure of $2\,\mu m \times 1\,\mu m \times 20$ nm sized rectangles made of permalloy [37] - the so-called standard problem #1 of micromagnetism. In contrast to simple reasoning, the angular histogram of the SEMPA dataset reveals not only the four domains of the expected Landau state, instead six domains are clearly separated. It turns out that the two larger domains along the long side of the rectangle are actually split along the short symmetry axis by some degrees, as shown in Fig. 17.3. This is a consequence of total energy minimization of the magnetic volume charge of the 180° wall along the center, which is compensated by surface charges along the edges of the structure. This tiny effect had previously been overlooked in the simulation, even though present, and it is responsible for the coupling between adjacent rectangles placed in a row, as the structures are no longer stray-field free. As the experimentally obtained splitting angle of 35° is much larger than the simulated 15° we adjusted the edge inclination and added edge roughness to obtain agreement. The additional effect of the contrast-enhancing iron layer on the coupling between rectangles was studied in [36].

Two studies deal with the ground state of domain walls in nanowires with a bend as function of bend angle, thickness and width [38], as well as a method to nucleate walls of fixed rotational sense in such bends [39]. Figure 17.4 shows as example the asymmetric transverse wall that is found in certain regions of parameter space instead
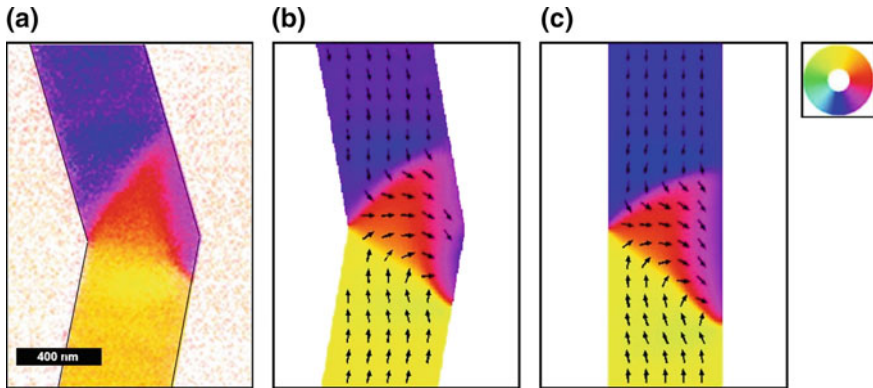
Fig. 17.4 Magnetic fine structure of an asymmetric transverse wall (ATW) in a soft-magnetic $Co_{39}Fe_{54}Si_7$ nanowire of width $w = 600\,nm$ and thickness $t = 10\,nm$. **a** SEMPA measurement of the ATW in a 30° bend. **b** OOMMF simulation of the exact geometry as in (**a**). **c** OOMMF simulation of an ATW in a straight section of the same wire. The local orientation of the magnetization is color coded according to the given color wheel. For details, see [38]

of symmetric transverse walls or vortex walls. These experiments form the basis of current and field driven domain wall displacement studies, as they allow to control and restore a selected starting configuration. Such an experiment was carried out with a permalloy nanowire on a liquid-nitrogen-cooled diamond substrate using the total magnetoresistance as probe for the magnetic state, while sweeping the external field as function of current density [22]. We found, that for permalloy there is no temperature dependence of the spin-torque efficiency over a temperature range from 77 to 327 K.

Furthermore, we analyzed the magnetic structure of the clean, single-crystalline Ni(111) surface and the effect of a graphene monolayer deposited on top [13]. In this multiscale, multitechnique approach, theory provided first-principles calculations of the spin-resolved band structure and spin-polarized STM analyzed low-temperature domain walls with close-to-atomic resolution. Using SEMPA, we performed the first vectorial imaging on this peculiar Ni surface, where no easy axis of the system is located. We could in principle confirm a multi-level branching of closure domains, that was predicted in [40]. The graphene layer in fact protected the surface magnetization of nickel against oxidation, so even after transfer at ambient conditions the domain pattern could be observed. We found a reduction of contrast, but no spin inversion for the secondary electrons after passing through the graphene.

17.4 Development of Time-Resolved SEMPA

Time-resolved magnetic microscopy is an essential tool to understand magnetization dynamics or to analyze switching processes in magnetic devices. Relevant timescales for LLG dynamics are in the sub-ns range, while ultrafast magnetization

dynamics concerns processes in the sub-ps range. Many techniques commonly used for static magnetic imaging can be empowered for time-resolved imaging by using a stroboscopic illumination with a source that can be periodically blanked, like a pulsed laser for scanning [41] or full-field [42] Kerr microscopy. Very recent developments have succeeded in transferring the time structure of a pump laser to an electron beam in a transmission electron microscope (TEM). The ultrafast Lorenz TEM uses a 150-femtosecond-laser-driven Schottky emitter [43] and the spin-polarized TEM [44] uses a picosecond-laser-pumped GaAs/GaAsP cathode. By synchronizing the illumination pulses with the periodically driven magnetization dynamics under investigation and varying the phase, a movie of the time evolution is obtained frame by frame. In scanning transmission X-ray microscopy (STXM), the internal bunch structure at a storage ring is used for illumination [45]. However, as here the illumination frequency is fixed, a more sophisticated measurement scheme is used, where the intensity information from each consecutive X-ray pulse is sorted by real-time electronics and accumulated into the according time slices. The synchronization here runs over an integer number of loops, so each revolution of the magnetic system is hit at different phases. In this way, all of the pulses can be used and maximum efficiency obtained.

17.4.1 Concept

To use time resolution in SEM, a stroboscopic approach with a blanked source or detector is in principle possible [46] and has already been used to record magnetic movies at microsecond time resolution [47]. However, due to the already long acquisition times per image this is not very attractive for SEMPA, as the time required to record a stroboscopic movie of n frames scales with n^2. Inspired by the STXM detection scheme, we came up with a much more efficient solution that does not even require in-vacuum modifications of the SEMPA (as long as high-frequency connections to the sample are already present) [18]. It is based on the fact that the SPLEED detector operates in single electron counting mode. Each electron of the four recorded LEED beams is amplified by a microchannel plate stack to give a 2 ns wide voltage pulse, that is normally only used for counting. Under the assumption of constant transit times for all electrons through the detector, the arrival time of each voltage pulse is just delayed by a constant with respect to the time the secondary electron was emitted at the sample surface. In this way the voltage pulses do not only carry the information about the local magnetization but also the information about the time at which this magnetic state was present. By using a periodic excitation and electronically recording the phase of all arriving voltage pulses with respect to this excitation, the counts can be grouped into time slices. In this way the whole time evolution at one pixel is recorded in parallel and with maximum efficiency, as (except for some timing overhead) all pulses are processed. A movie of the time evolution of a whole magnetic object is then recorded by scanning pixel after pixel.
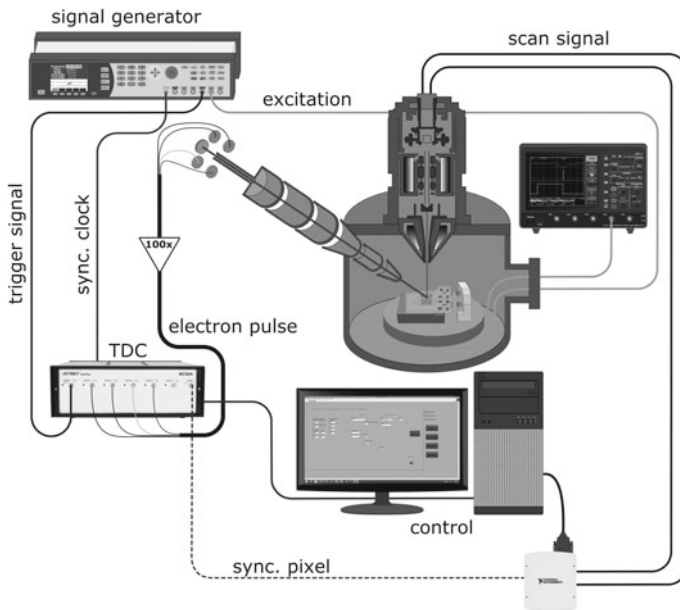
Fig. 17.5 Sketch of the setup used for TR-SEMPA. The time-to digital converter (TDC) receives the amplified voltage pulses from the SPLEED detector. A synchronized signal generator drives a current through the sample and the transmitted voltage is monitored using a scope. For details, see [18]

For this detection scheme the time to record n frames scales linearly with n, which is normally of the order of hours and thus feasible.

17.4.2 Experimental Setup

A sketch of the experimental setup for TR-SEMPA is given in Fig. 17.5. The only new hardware required is a time-to-digital converter (TDC) that measures the arrival time of each voltage pulse with respect to a trigger signal that is generated from the signal generator driving the magnetization dynamics. We use a four-channel TDC with 100 ps time resolution that transmits the digital data for all the pulses in real-time to a computer for on-line processing.

The sample used in the demonstration experiment is a 60 nm thick and 3.5 μm wide square made from soft-magnetic amorphous $Fe_{70}Co_8Si_{12}B_{10}$ [48]. The square is in its magnetic Landau ground state. It is deposited onto a gold (150 nm)/chromium (24 nm) microstrip of 5 μm width on a sapphire substrate. An electrical current running along the microstrip gives rise to an Oersted field across the strip and thus shifts the magnetic vortex of the Landau structure to the left or right.
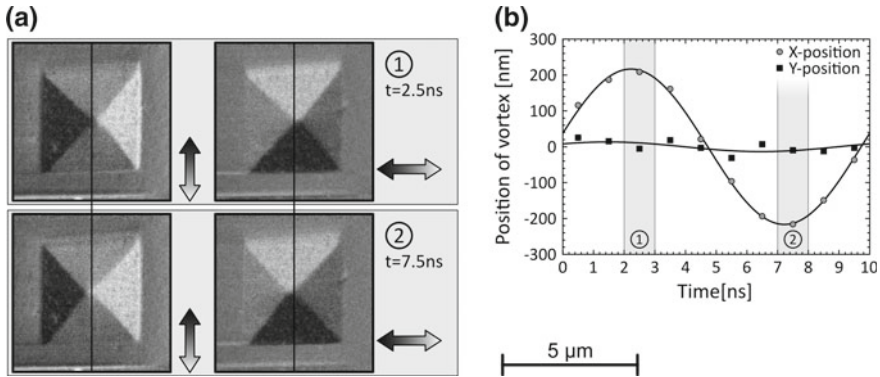
Fig. 17.6 Field-driven vortex oscillation in the Landau state of a soft-magnetic square element. The 60 nm thick and 3.5 μm wide square has been prepared from $Fe_{70}Co_8Si_{12}B_{10}$ on a gold microstrip. The Oersted field from a sine-modulated current at 100 MHz running horizontally in the microstrip is used to drive the dynamics. Panel **a** shows two selected frames of 1 ns duration from a 10-frame movie. The SEMPA micrographs give the vertical and horizontal magnetization components at maximum positive (delay 2.5 ns) and negative (delay 7.5 ns) displacements. Dashed lines indicate the horizontal zero-position around which the vortex oscillates. In **b** the horizontal and vertical coordinates of the vortex have been extracted from the movie. For details, see [18]

17.4.3 Results and Analysis

Figure 17.6 shows two frames at the positions of maximum displacement from a 10-frame movie acquired with TR-SEMPA. The sample was driven with a 100 MHz sine current. A sine displacement along the horizontal axis with 440 μm peak-to-peak amplitude is observed in the movie. The corresponding vortex positions have been extracted and are plotted in panel (b). Surprisingly, the vertical displacement is only at the noise limit, so the gyration that would be expected not too far from nominal resonance is strongly suppressed. An analysis of the dynamics in this structure, when driven at different frequencies, reveals that the suppression of gyration corresponds to the behavior of an oscillator with strongly damped dynamics. Cross-sections of the structure suggest that the damping is of extrinsic nature and can be attributed to a very rough surface of the gold microstrip, that was copied during deposition into the magnetic film.

From the high-quality image, not only the position of the vortex can be extracted but the full vectorial map, which shows the same image quality as a static SEMPA image at this relative acquisition time, is accessible in a time-resolved way. For instance, in this example the motion of the 90° bends can be studied in detail.

The time resolution available in this experiment has been determined from the motion blur effect of a sample edge, that is rapidly shifting when a square-wave modulation of the sample potential is performed. The sample edge gets widened (blurred) as a function of apparent velocity, as can be extracted from line profiles. Quantitative analysis yields a time resolution of (720 ± 80) ps [18]. Electron-optical

simulation reveals that this resolution is to be expected with the design parameters of the currently used spin detector. The energy and angular distributions of the secondary electrons at the time of emission from the sample surface lead to a jitter in transit time through the spin detector, that smears out the correlation between starting time and pulse detection.

17.5   Conclusion and Outlook

The application of high-resolution vectorial magnetic imaging has been very successful in resolving a large number of open questions. Especially, we could confirm the importance of non-local effects when describing the current-driven dynamics of vortices in contrast to more extended objects. With the invention of TR-SEMPA we have opened a new experimental access to study magnetization dynamics that preserves all the advantages of stationary SEMPA, especially the ability to work on ideal epitaxial samples on single-crystalline substrates. This will allow to study dynamical processes in pure elements that are free from pinning at grain boundaries and show the unaltered behavior that can be directly compared to first principles calculations. Technologically more relevant are, however, glassy alloys containing, for instance, boron, where grain growth is suppressed.

Already for some time the interest in the community has shifted away from in-plane systems for spintronic devices towards out-of-plane magnetized systems. Especially if these are prepared in the form of artificially layered antiferromagnets [49], such that the stray field interaction is fully compensated, a much closer packing of structures and therefore of information can be obtained. In addition to the STT discussed here, new and more efficient torque terms appear in current-driven dynamics that can sustain higher domain wall velocities up to 750 m/s [50], which are required for application. These spin-orbit torques can result from Rashba effects or the inverse spin-Hall effect and open the promising field of spin-orbitronics. With the new SEMPA setup with out-of-plane sensitivity this class of materials can be analysed. The high surface sensitivity warrants, that only the topmost layer of an antiferromagnetically coupled stack contributes to the contrast, so that the full magnetic signal is available.

In addition to the geometry that has changed over the course of years, also a new class of magnetic particles has today strongly moved into the focus of research. Instead of domain walls, magnetic interface skyrmions, are envisioned for use in magnetic wires instead of domain walls to carry and store information [51]. They are topologically protected against spontaneous decay and get repelled from wire boundaries and by each other. Interface skyrmions were observed for the first time by low-temperature SP-STM on epitaxial Fe/Ir(111) [52]. The key to stabilizing such skyrmions at room temperature is a strong interfacial Dzyaloshinskii-Moriya interaction (DMI) that can typically be found at non-symmetric interfaces between ferromagnets and materials with strong spin-orbit coupling.
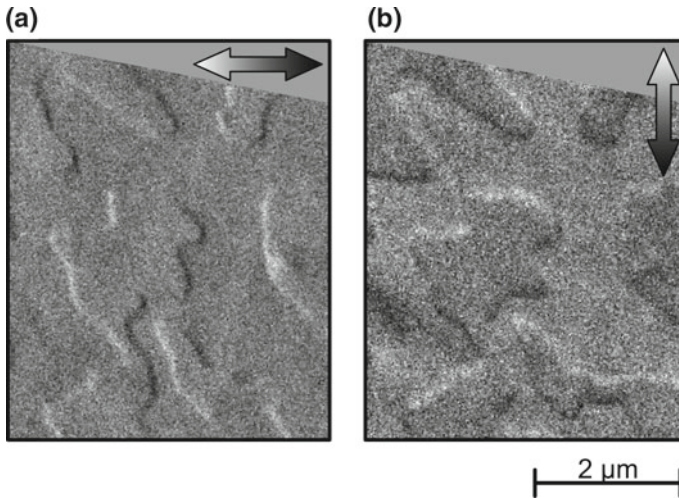
Fig. 17.7 SEMPA measurement of an epitaxial Co/Pt(111) layer at 1.4 nm thickness. All domain walls show a pure Néel character with fixed anticlockwise rotational sense, indicative of a positive DMI. From a quantitative analysis upper and lower bounds for the DMI strength have been derived. For details, see [53]

Recently we have obtained results on SEMPA imaging of such DMI systems by analysing the domain wall angles in epitaxially grown, uncapped cobalt on a Pt(111) single crystal surface [53]. The single layer Co films were grown as a wedge, so that thicknesses from 0 to 1.5 nm were accessible. From LEED data it is clear that the DMI-generating interface layer of Co grows pseudomophically; at higher coverage the growth becomes less ideal. The analysis of SEMPA data shows that over the whole out-of-plane magnetized range all domain walls are of pure Néel character. In addition, all domain walls show a fixed counterclockwise rotational sense, indicating a positive sign of the DMI (see Fig. 17.7). Even though the DMI is an interface effect it still dominates the energy balance of the domain walls, where otherwise uncharged Bloch walls would be favored. From the domain wall energy balance at 1.4 nm coverage a lower bound of 0.8 eV per interface Co atom for the DMI strength was calculated. The observation of a multi-domain state even at the onset of ferromagnetism at 0.3 nm allows to deduce an upper bound of 4.3 meV per interface Co atom. These findings confirm previous first-principles calculations.

Another study on DMI materials focussed on ex-situ-prepared multilayer films [54]. Multilayers consisting of several repeats of Co/Pt/Ir are considered as good candidates for room-temperature skyrmions because the DMI of both interfaces is of opposite sign and thus the total DMI adds up. We have shown, that 150 eV argon ion sputtering can be used to mill away the topmost Pt layer and to image the rotational sense of domain walls in such systems. A second method introduced is the deposition of a thin iron layer onto the topmost Pt layer. The iron layer shunts the magnetic flux of the out-of-plane magnetized domains underneath thus yielding an in-plane contrast.

By calculating the divergence of the in-plane SEMPA map the domain structure of the out-of-plane domains in the Co/Pt/Ir system becomes visible. We confirmed that both methods did not alter the magnetic state of the multilayer.

References

1. J. Grollier, D. Lacour, V. Cros, A. Hamzic, A. Vaurès, A. Fert, D. Adam, G. Faini, J. Appl. Phys. **92**(8), 4825 (2002)
2. M. Kläui, C.A.F. Vaz, J.A.C. Bland, W. Wernsdorfer, G. Faini, E. Cambril, L.J. Heyderman, Appl. Phys. Lett. **83**(1), 105 (2003)
3. M. Tsoi, R. Fontana, S. Parkin, Appl. Phys. Lett. **83**(13), 2617 (2003)
4. A. Yamaguchi, T. Ono, S. Nasu, K. Miyake, K. Mibu, T. Shinjo, Phys. Rev. Lett. **92**(7), 077205 (2004)
5. S.S.P. Parkin, M. Hayashi, L. Thomas, Science **320**(5873), 190 (2008)
6. L. Berger, J. Appl. Phys. **55**, 1954 (1984)
7. J.C. Slonczewski, J. Magn. Magn. Mater. **159**, L1 (1996)
8. S. Zhang, Z. Li, Phys. Rev. Lett. **93**(12), 127204 (2004)
9. G. Tatara, H. Kohno, Phys. Rev. Lett. **92**(8), 086601 (2004)
10. A. Thiaville, Y. Nakatani, J. Miltat, Y. Suzuki, Europhys. Lett. **69**(6), 990 (2005)
11. B. Krüger, M. Najafi, S. Bohlens, R. Frömter, D.P.F. Möller, D. Pfannkuche, Phys. Rev. Lett. **104**(7), 077201 (2010)
12. S. Rößler, S. Hankemeier, B. Krüger, F. Balhorn, R. Frömter, H.P. Oepen, Phys. Rev. B **89**, 174426 (2014)
13. L.V. Dzemiantsova, M. Karolak, F. Lofink, A. Kubetzka, B. Sachs, K. von Bergmann, S. Hankemeier, T.O. Wehling, R. Frömter, H.P. Oepen, A.I. Lichtenstein, R. Wiesendanger, Phys. Rev. B **84**, 205431 (2011)
14. S. Rößler, Magnetic imaging of static and dynamic states in systems of reduced dimensions. (Shaker, Aachen, 2015)
15. H.P. Oepen, R. Frömter, *Handbook of Magnetism and Advanced Magnetic Materials* (Wiley, New York, 2007). Chap. Scanning Electron Microscopy with Polarization Analysis
16. R. Frömter, S. Hankemeier, H.P. Oepen, J. Kirschner, Rev. Sci. Instrum. **82**(3), 033704 (2011)
17. F. Lofink, S. Hankemeier, R. Frömter, J. Kirschner, H.P. Oepen, Rev. Sci. Instrum. **83**, 023708 (2012)
18. R. Frömter, F. Kloodt, S. Rößler, A. Frauen, P. Staeck, D.R. Cavicchia, L. Bocklage, V. Röbisch, E. Quandt, H.P. Oepen, Appl. Phys. Lett. **108**, 142401 (2016)
19. B. Krüger, A. Drews, M. Bolte, U. Merkt, D. Pfannkuche, G. Meier, Phys. Rev. B **76**(22), 224426 (2007)
20. S. Barman, G.P. Srivastava, J. Appl. Phys. **101**(12), 123507 (2007)
21. S. Hankemeier, K. Sachse, Y. Stark, R. Frömter, H.P. Oepen, Appl. Phys. Lett. **92**(24), 242503 (2008)
22. B. Beyersdorff, S. Hankemeier, S. Rößler, Y. Stark, G. Hoffmann, R. Frömter, H.P. Oepen, B. Krüger, Phys. Rev. B **86**(18), 184427 (2012)
23. L. Heyne, J. Rhensius, D. Ilgaz, A. Bisig, U. Rüdiger, M. Kläui, L. Joly, F. Nolting, L.J. Heyderman, J.U. Thiele, F. Kronast, Phys. Rev. Lett. **105**, 187203 (2010)
24. S. Pollard, L. Huang, K. Buchanan, D. Arena, Y. Zhu, Nat. Commun. **3**, 1028 (2012)
25. K. Sekiguchi, K. Yamada, S.M. Seo, K.J. Lee, D. Chiba, K. Kobayashi, T. Ono, Phys. Rev. Lett. **108**, 017203 (2012)
26. G. Tatara, P. Entel, Phys. Rev. B **78**, 064429 (2008)
27. K.J. Lee, M. Stiles, H.W. Lee, J.H. Moon, K.W. Kim, S.W. Lee, Phys. Rep. **531**(2), 89 (2013)
28. D. Claudio-Gonzalez, A. Thiaville, J. Miltat, Phys. Rev. Lett. **108**, 227208 (2012)

29. V. Volkov, Y. Zhu, M.D. Graef, Micron **33**(5), 411 (2002)
30. R.E. Dunin-Borkowski, T. Kasama, A. Wei, S.L. Tripp, M.J. Hÿtch, E. Snoeck, R.J. Harrison, A. Putnis, Microsc. Res. Techn. **64**(5–6), 390 (2004)
31. A. Drews, Fast Micromagnetic Simulator for Computations on Cpu and Graphics Processing Unit (gpu) (2014)
32. M.J. Donahue, D.G. Porter, *Interagency Report NISTIR 6376* (National Institute of Standards and Technology, MD, 1999)
33. R. Frömter, H. Stillrich, C. Menk, H.P. Oepen, Phys. Rev. Lett. **100**, 207202 (2008)
34. M. Seifert, L. Schultz, R. Schäfer, S. Hankemeier, R. Frömter, H.P. Oepen, V. Neu, New J. Phys. **19**(3), 033002 (2017)
35. M. Seifert, L. Schultz, R. Schäfer, V. Neu, S. Hankemeier, S. Rößler, R. Frömter, H.P. Oepen, New J. Phys. **15**(1), 013019 (2013)
36. J. Jelli, K.M. Lebecki, S. Hankemeier, R. Frömter, H.P. Oepen, U. Nowak, IEEE Trans. Magn. **49**(3), 1077 (2013)
37. S. Hankemeier, R. Frömter, N. Mikuszeit, D. Stickler, H. Stillrich, S. Pütter, E.Y. Vedmedenko, H.P. Oepen, Phys. Rev. Lett. **103**(14), 147204 (2009)
38. F. Lofink, A. Philippi-Kobs, M.R. Rahbar Azad, S. Hankemeier, G. Hoffmann, R. Frömter, H.P. Oepen, Phys. Rev. Appl. **8**, 024008 (2017)
39. S. Hankemeier, A. Kobs, R. Frömter, H.P. Oepen, Phys. Rev. B **82**, 064414 (2010)
40. A. Hubert, R. Schäfer, *Magnetic Domains: The Analysis of Magnetic Microstructures* (Springer, Berlin, 2009)
41. W.K. Hiebert, A. Stankiewicz, M.R. Freeman, Phys. Rev. Lett. **79**(6), 1134 (1997)
42. N.O. Urs, B. Mozooni, P. Mazalski, M. Kustov, P. Hayes, S. Deldar, E. Quandt, J. McCord, AIP Adv. **6**(5), 055605 (2016)
43. T. Eggebrecht, M. Möller, J.G. Gatzmann, N. Rubiano da Silva, A. Feist, U. Martens, H. Ulrichs, M. Münzenberg, C. Ropers, S. Schäfer, Phys. Rev. Lett. **118**, 097203 (2017)
44. M. Kuwahara, Y. Nambo, K. Aoki, K. Sameshima, X. Jin, T. Ujihara, H. Asano, K. Saitoh, Y. Takeda, N. Tanaka, Appl. Phys. Lett. **109**(1), 013108 (2016)
45. Y. Acremann, V. Chembrolu, J.P. Strachan, T. Tyliszczak, J. Stöhr, Rev. Sci. Instrum. **78**, 014702 (2007)
46. G.S. Plows, W.C. Nixon, J. Phys. E **1**(6), 595 (1968)
47. T. Ikuta, R. Shimizu, J. Phys. E **9**(9), 721 (1976)
48. V. Hrkac, E. Lage, G. Köppel, J. Strobel, J. McCord, E. Quandt, D. Meyners, L. Kienle, J. Appl. Phys. **116**(134302) (2014)
49. S. Parkin, S.H. Yang, Nat. Nano **10**(3), 195 (2015)
50. S.H. Yang, K.S. Ryu, S. Parkin, Nat. Nano **10**(3), 221 (2015)
51. A. Fert, V. Cros, J. Sampaio, Nat. Nanotechnol. **8**, 152 (2013)
52. S. Heinze, K. von Bergmann, M. Menzel, J. Brede, A. Kubetzka, R. Wiesendanger, G. Bihlmayer, S. Blügel, Nat. Phys. **7**, 713 (2011)
53. E.C. Corredor, S. Kuhrau, F. Kloodt-Twesten, R. Frömter, H.P. Oepen, Phys. Rev. B **96**, 060410(R) (2017)
54. J. Lucassen, F. Kloodt-Twesten, R. Frömter, H.P. Oepen, R.A. Duine, H.J.M. Swagten, B. Koopmans, R. Lavrijsen, Appl. Phys. Lett. **111**(13), 132403 (2017)